

Supersonically sprayed carbon nanotubes and silver nanowires as efficient heat spreaders and cooling films

Cite as: J. Appl. Phys. **127**, 105105 (2020); <https://doi.org/10.1063/1.5144167>

Submitted: 27 December 2019 . Accepted: 22 February 2020 . Published Online: 11 March 2020

Tae-Gun Kim, Chan-Woo Park, Yong-il Kim, Ali Aldalbahi , Mostafizur Rahaman, and Sam S. Yoon 



View Online



Export Citation



CrossMark

Lock-in Amplifiers
Find out more today



 Zurich
Instruments



Supersonically sprayed carbon nanotubes and silver nanowires as efficient heat spreaders and cooling films

Cite as: J. Appl. Phys. 127, 105105 (2020); doi: 10.1063/1.5144167

Submitted: 27 December 2019 · Accepted: 22 February 2020 ·

Published Online: 11 March 2020



Tae-Gun Kim,¹ Chan-Woo Park,¹ Yong-il Kim,¹ Ali Aldalbahi,²  Mostafizur Rahaman,² and Sam S. Yoon^{1,a)} 

AFFILIATIONS

¹School of Mechanical Engineering, Korea University, Seoul 136-713, South Korea

²Department of Chemistry, College of Science, King Saud University, Riyadh 11451, Saudi Arabia

^{a)}Author to whom correspondence should be addressed: skyoona@korea.ac.kr

ABSTRACT

With the ever-decreasing size of portable electronics to achieve greater versatility, the power density of electronic devices has increased substantially, to the point where efficient cooling has become a major concern for achieving stable device operation. Herein, we introduce a heat-dissipating film coated with carbon nanotubes (CNTs) entangled with silver nanowires (AgNWs), prepared by supersonic spraying. Low thermal resistance was obtained from the strong adhesion between the deposited nanomaterials and the substrate. The optimal hybrid film for achieving maximal cooling was identified by varying the number of spraying sweeps and the composition of the nanomaterials. The hybrid film, comprising both CNTs and AgNWs, afforded superior cooling owing to its improved thermal conductivity. Surface-texturing of the film also significantly impacted the convective-cooling performance. In addition, the superior heat-spreading capability of the hybrid film was demonstrated by comparing infrared images of the bare substrate, pure CNTs, and hybrid CNT/AgNW films. The wettability of these films was also studied to identify the wetting condition that would provide the maximum heat transfer. The hybrid CNT/AgNW film possessed the most hydrophilic surface, providing the most efficient spray-cooling scenario. The hydrophilic surface captured and held the sprayed droplets firmly throughout the process. Hence, these CNT/AgNW hybrid films represent a commercially viable solution for addressing hotspots in portable electronic devices.

Published under license by AIP Publishing. <https://doi.org/10.1063/1.5144167>

I. INTRODUCTION

The demand for miniaturization of portable electronics with versatile features inevitably requires high-power-density or high-flux microprocessors, which eventually leads to heat-induced malfunctions in devices.^{1–5} Such device-heating concerns are often initiated by local hotspots or fireballs, wherein the power density can reach up to 10^3 W cm^{-2} .^{6–9}

Traditional cooling methods require the introduction of fans, heat pipes, heatsinks, and thermoelectric coolers into electronic devices.^{6,8,10–19} These inclusions lead to other issues, such as additional weight, volume, noise, extra power sources, complexities in installation, and reliability issues. Therefore, the development of light, small, attachable, fan-free, and heatsink-free cooling films is necessary to facilitate the production of more commercially viable and practical cooling films.

One practical way to achieve this goal is to increase the total surface area of the film by introducing nanotextured surfaces on the film, without using fans or heatsinks. This approach may afford an enhancement in the total surface area per unit volume and hence would increase the convective-heat-transfer coefficient.²⁰ Furthermore, the textured surface can be decorated with nanomaterials having high thermal conductivity, which would lower the thermal resistance of the film. In general, there are two ways of alleviating hotspots. First, the heat generated at the hotspot can be directly removed via convective cooling. Second, the heat can be spread via conduction. The latter approach is the only way to alleviate hotspot formation in electronics that are completely sealed for waterproofing. In this scenario, inflow or outflow is not permitted, and thus, direct convective cooling is not possible. Heat-spreading via conduction is the only alternative for alleviating the thermal stress due to hotspots. Therefore, cooling films having high thermal

conductivity and diffusivity are desired. Recently, theoretical studies on thermal conduction through amorphous solids, graphene, and glassy diamond via phonon scattering have been documented.^{21–23}

Herein, we aim to increase the convective-heat-transfer coefficient by introducing a textured surface created using carbon nanotubes (CNTs). These CNTs can be decorated with silver nanowires (AgNWs) to ensure that the cooling film can efficiently spread heat via conduction.²⁴ The inclusion of CNTs facilitates efficient convection, while the incorporation of AgNWs affords efficient conduction. Moreover, the CNT itself, by virtue of its high thermal conductivity, lowers the thermal resistance of the film.^{25–31} To the best of our knowledge, CNT/AgNW composites have never been used as heat-spreading materials. Similar carbon-encased nanomaterials have been utilized as thermal-interface materials to cool electronic devices.^{26,32–37} However, incorporating these nanomaterials on the surface of electronics often requires additives, which are another source of thermal insulation, hindering efficient heat transfer. Therefore, the development of a coating method that facilitates the deposition of these nanomaterials without the use of additives is imperative.

Supersonic cold-spraying is an efficient method of depositing nanomaterials without the use of additives.^{38–41} Nanomaterials are enclosed inside atomized droplets and transported at supersonic speeds, during which the liquid in the droplet evaporates. Thus, only the remaining dry nanomaterials are deposited on the substrate, to which they are strongly adhered and bonded. This method precludes the introduction of impurities, which might adversely affect the cooling performance of the film. Furthermore, this method does not require any post-annealing processes that allow the use of flexible substrates. In addition, cold-spraying is scalable and is, therefore, suitable for mass production on a commercial scale.

In this study, cold-spraying is used to first deposit CNTs with various film thicknesses on an alumina substrate. Thereafter, the optimal film thickness affording the lowest thermal resistance and best convective cooling is identified. The optimal CNT composite is further combined with AgNWs to achieve a further reduction in the thermal resistance.

II. EXPERIMENTAL

A. Supersonic spraying

The supersonic cold-spraying system consists of a gas compressor, a gas heater, and a converging–diverging nozzle (De Laval nozzle) from which a supersonic flow is generated. The atomizer produces droplets enclosing the nanomaterials, which are entrained into the supersonic stream.^{38–40,42–44} In general, air is used as the working gas; the air is compressed to 0.4 MPa by the gas compressor, heated to 250 °C upon passing through the gas heater, and then supplied to the nozzle to create a supersonic flow.

The CNT solution was prepared by adding 0.1 g of CNT (XNM-HP15000, XinNano Materials Inc.) to a precursor solution comprising 40 ml of *N,N*-dimethylformamide (DMF, Sigma-Aldrich) and 0.3 ml of 8 wt. % polyacrylonitrile (PAN; Sigma-Aldrich, average $M_w = 150\,000$). The precursor solution was injected into an atomizer (VCS 40 kHz, Sonics & Materials) by a syringe pump (Legato 210, KDS) at a flow rate of 1.5 ml min⁻¹. The AgNWs (average diameter = 20 nm; length = 15 μm) were dispersed in 30 ml of isopropyl alcohol (IPA, Duksan, Korea) at a concentration of 0.15 wt. %. This CNT/AgNW mixture ratio was selected to sufficiently cover the film surface with AgNWs, as visually confirmed using scanning electron microscopy (SEM); this optimal mixture ratio was determined by trial-and-error. The supersonically sprayed CNT/AgNWs adhered firmly to various types of substrates, without the need for additives.

B. Fabrication of heat spreader

Figure 1 illustrates the procedure for fabricating the cooling films. A nickel–chrome (Ni–Cr) heating wire was inserted and sandwiched between two Al₂O₃ substrates, as shown in Fig. 1(a). The Ni–Cr wire was supplied with $9 \leq q \leq 18$ W of power. Figure 1(b) shows the feed of the CNT solution through the atomizer toward the supersonic nozzle. The atomized droplets were sprayed in the direction of the Al₂O₃ substrate. Figure 1(b) also shows a similar fabrication process, except that in this case,

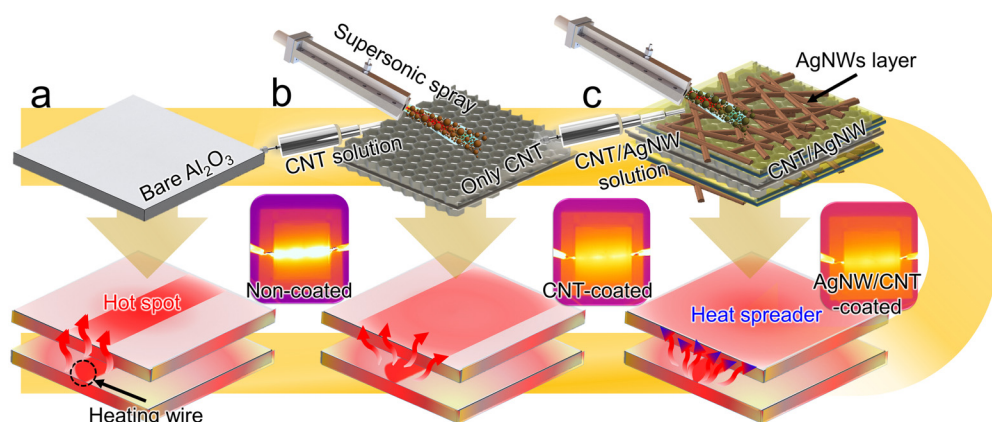


FIG. 1. Detailed schematic of the cooling test module. (a) Heating wire sandwiched between Al₂O₃ substrates, (b) CNT-coated Al₂O₃ substrates, and (c) CNT/AgNW-coated Al₂O₃ substrates.

the precursor was mixed with AgNWs, and, therefore, CNT/AgNWs were coated onto the Al_2O_3 substrate. The corresponding infrared images are included in Fig. 1 as an inset, showing the temperature distribution of the films subjected to a power of $q = 18$ W. The CNT/AgNWs provided the most uniform temperature distribution.

C. Heat-transfer experiment

Figure 2 shows the series of setups for the heat-transfer experiments. A direct current (DC) power supply (E3644A, Agilent Tech, USA) with a maximum output power of 60 W was used to supply heat in the range of $9 \leq q \leq 18$ W. The error margin of the applied voltage and current were confirmed to be $0.1\% \pm 150$ mV and ± 15 mA, respectively. Using a DC power supply, a voltage was applied to each end of the heating wire located between the Al_2O_3 substrates. The resistance of the wire was approximately $5.73 \Omega \text{ m}^{-1}$ and the diameter was approximately 0.5 mm. The temperatures at all points (T_1 and T_2) were recorded using a temperature data logger (GL-240, Graphtech, USA) and K-type thermocouples (probe size of 1×150 mm², uncertainty of ± 0.5 °C). The total level of uncertainty in the amount of heat transferred to the wire was estimated to be 1.6%, using the error-propagation method.⁴⁵ To minimize the heat loss, heat was transferred only to the top layer, while the bottom substrate was well-insulated. The conductive heat loss through the bottom substrate, estimated from the temperature difference between the bottom substrate and the insulation, was less than 1%. The surface area and the surrounding environment at the top surface of the heat spreader promoted convective cooling. As shown in Fig. 2(b), the heat spreader was also covered with aluminum foil to minimize radiative heat loss.

The thermal conductivity of the fabricated cooling films was measured using the standard ASTM E1461 (ASTM International, thru-plane) method. In this method, the thermal conductivity is calculated by measuring the thermal diffusivity, which can be estimated using the following equation: $k \approx \lambda \rho C_p$, where λ is the thermal conductivity, ρ is the density, and C_p is the specific heat capacity. The measurable range is 0.1 – 2000 $\text{W m}^{-1} \text{ K}^{-1}$.

D. Characterization

High-resolution SEM (HR-SEM at 15 kV, XL30 SFEQ, Phillips Co., Netherlands), a non-contacting 3D optical profiler (OP) (NT, Veeco, USA), and transmission electron microscopy (TEM, JEM 2100F, JEOL, Inc.) were used to evaluate the morphology and roughness of the surface of the multilayer heat spreader.

An infrared (IR) camera (FLIR-E63900, FLIR System, Inc.) was also used to visualize the transfer of heat over time. The IR camera had a thermal sensitivity of 30 mK at room temperature ($T_\infty = 25$ °C), with an uncertainty level of approximately $\pm 1\%$. The IR camera was initially calibrated by measuring the temperature of an object at 25 °C, where the temperature was confirmed against that measured using a thermocouple. The temperature from the thermocouple measurement was synchronized with that from the IR image by adjusting the emissivity, ε . The emissivity of the IR camera was adjusted to $\varepsilon = 1$ to avoid residual heat from other surrounding sources.

III. RESULTS AND DISCUSSION

Figure 3 presents a comparison of the temperatures of the Ni-Cr heating wire (T_1) in the various films: $N = 0, 5, 10,$ and 20 . The $N = 0$ label refers to the bare substrate, while the $N > 0$ cases refer to the substrate coated with CNTs using different numbers of spray passes (without AgNWs). The supplied heat was increased from $q = 9$ W to 18 W [Figs. 3(a)–3(d)]. The wire temperature (T_1) increased over the time span of 1200 s. Higher temperatures were observed when the substrate was subjected to greater heat (q), reaching the highest temperature of $\Delta T = T_1 - T_\infty \approx 95$ °C at $t = 1200$ for $q = 18$ W.

T_1 was the highest at $N = 0$, as shown in Fig. 3(a). The highest wire temperature, T_1 , was observed for the sample without nanotexturing, owing to the superior cooling effect in the nanotextured samples ($N > 0$). For example, T_1 was the lowest at $N = 10$ for all q values, implying that the nanotexturing was optimal at $N = 10$. However, at $N = 20$, T_1 again increased owing to thickening of the CNT layer. In general, when the film thickness increases at a steady state, the bottom-film temperature (T_1) inevitably increases to maintain a constant heat flux (q). This thickness factor, which invariably increases T_1 , becomes more prominent as q increases. Figures 3(b)–3(d) show that T_1 was the greatest when $N = 20$. This pattern indicates that cooling via nanotexturing was no longer effective when the film thickness exceeded $N > 10$. When the film is sufficiently thick, the thickness effect dominates the cooling effect, which is undesirable. Therefore, the film thickness must be minimized while maximizing the texturing effect, by finding the optimal film thickness to achieve a suitable balance. In this study, the optimal film thickness was achieved at $N = 10$, which was consistently the case for all values of q .

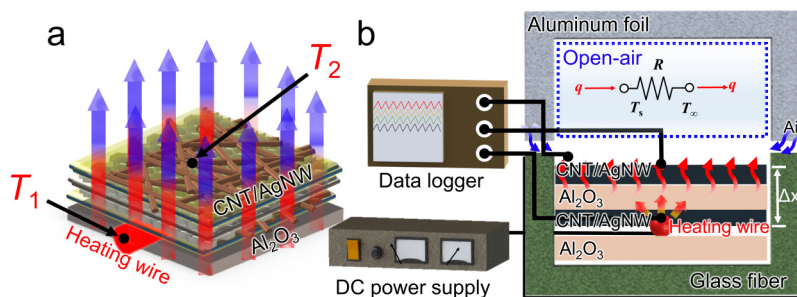


FIG. 2. Detailed schematics of (a) heat spreader comprising multiple layers of CNTs and AgNWs, (b) insulated heat spreader used in the heat-transfer experiment.

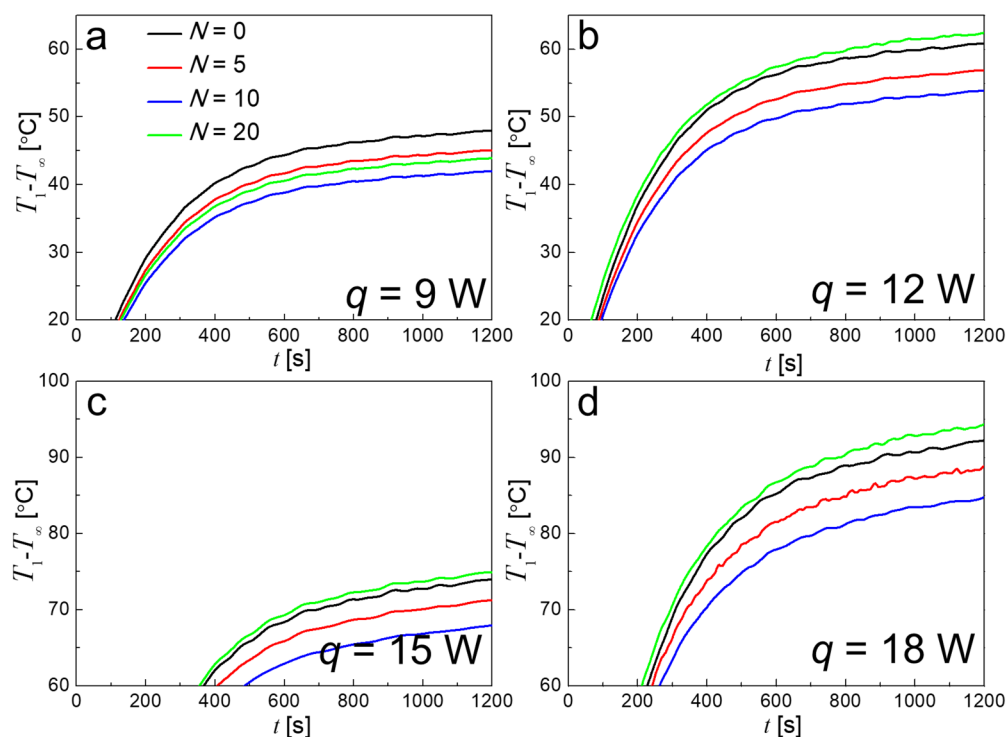


FIG. 3. Heating-wire temperature (T_1) vs time. Effect of the number of spray passes (N) with the variation of the heating power: (a) $q=9$ W, (b) 12 W, (c) 15 W, and (d) 18 W.

Figure 4 presents a qualitative comparison of the IR images of the fabricated films that were subjected to the same heat at $q = 18$ W. The Ni–Cr heating wire was visible at the centerline of the films at $t = 10$ s. Initially, there was no significant difference

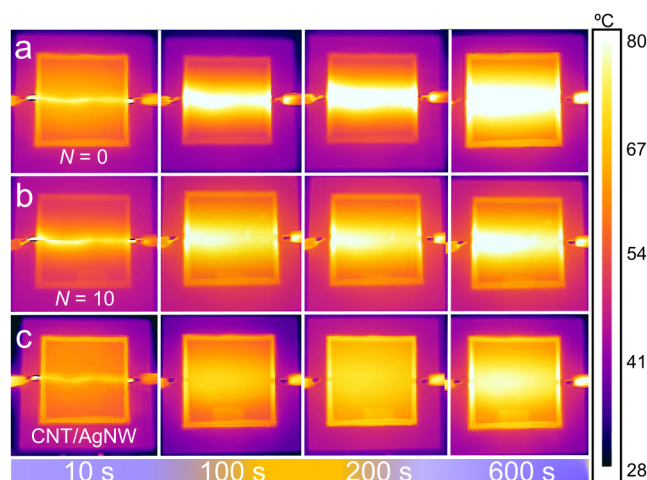


FIG. 4. IR images of heated CNT films for (a) $N=0$ (bare), (b) $N=10$ (CNT only), and (c) $N=10$ (CNT/AgNW) films at $q = 18$ W.

between the temperature distributions of various films. However, the temperature gradient was the most pronounced for $N=0$ (bare) as the heat spread. For $N=0$, a bright centerline hotspot was apparent, confirming inefficient heat spread. In contrast, for $N=10$ (CNT) [Fig. 4(b)], the overall temperature gradient was relatively uniform, unlike for the $N=0$ case [Fig. 4(a)], this is attributed to improved convective cooling due to the CNT coating layers. Figure 4(c) confirms that the CNT/AgNW hybrid film produced the most uniform temperature distribution, demonstrating the most effective heat spread.

Figure 5 presents the SEM and optical profiler (OP) images for the samples synthesized with $N=5$, 10, and 20 spray passes. The film thickness increased from $d = 6.57$ to $13.78 \mu\text{m}$ as the number of spray passes increased from $N=5$ to 20. The surface roughness of the film also increased from $R_a = 0.9$ to $2.8 \mu\text{m}$ with increasing N . This increased roughness enhanced the convection cooling by increasing the heat-transfer activity owing to the increased total surface area. However, as depicted in Fig. 3, convection cooling and thermal insulation present competing effects when the surface area and film thickness are, respectively, changed. Increasing the film thickness by increasing N inherently increases the Ni–Cr wire temperature (T_1) via thermal insulation, while convective cooling is enhanced by the increased surface area. Therefore, a compromise regarding the film thickness must be made to achieve optimal cooling. The magnified SEM images in Fig. 5 (first column) show that the CNTs were agglomerated into slabs, the collection of which

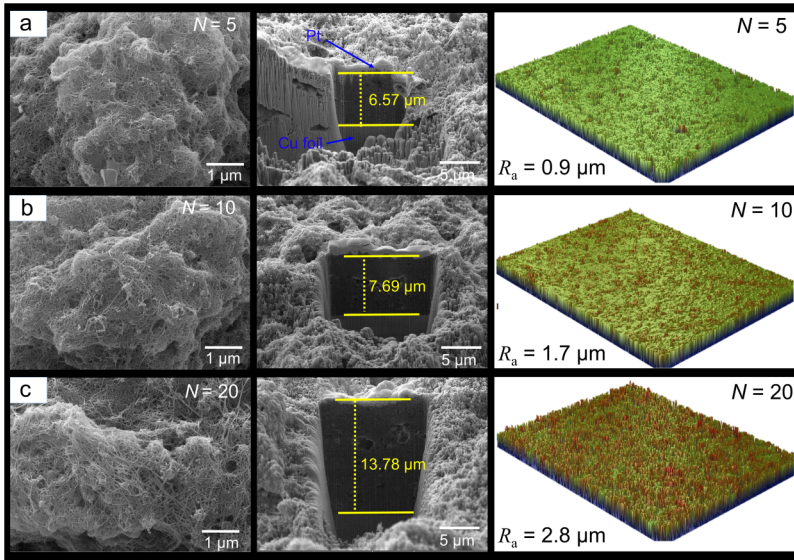


FIG. 5. SEM (left: surface; middle: cross section) and optical profiler (OP) images of CNT films for (a) $N = 5$, (b) $N = 10$, and (c) $N = 20$.

led to differences in the surface roughness with the variation of N . Although N did not appear to alter the distribution of the CNTs over the surface area, changing N altered the surface roughness, as shown in the OP images in Fig. 5 (third column).

Figure 6(a) presents an outline of the electrical circuit model for the CNT-coated films. The heat flux, q , moves through the CNT-coated layer (R_1) and eventually flows to the open air (R_2) in the normal (or axial) direction. The heat-transfer phenomena for R_1 and R_2 are modeled using Fourier's law and Newton's cooling law for a quasi-1D analysis, respectively. These models are

represented as follows:

$$q = \frac{T_1 - T_2}{R_1}, \quad R_1 = \frac{\Delta x}{kA_p}, \quad (1)$$

$$q = \frac{T_2 - T_\infty}{R_2}, \quad R_2 = \frac{1}{h_{\text{eff}}A_p}, \quad (2)$$

where Δx (in m) is the thickness of the CNT layer, k is the thermal conductivity (in $\text{W m}^{-1} \text{K}^{-1}$), A_p is the projected substrate area

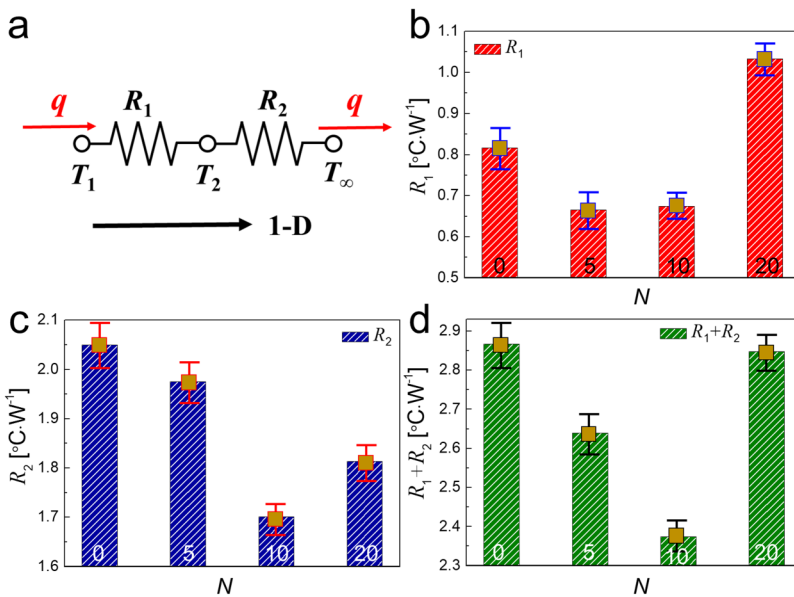


FIG. 6. (a) Electrical circuits depicting the average thermal resistance across the solid layer (from T_1 to T_2) and convective air cooling (from T_2 to T_∞) in the normal direction. (b) Relative thermal resistance across the solid layers, R_1 . (c) Relative thermal resistance through open air, R_2 . (d) Sum of R_1 and R_2 . The thermal resistance was averaged over all values; $q = 9, 12, 15, \text{ and } 18 \text{ W}$.

(in m^2), and h_{eff} (in $\text{W m}^{-2} \text{K}^{-1}$) is the effective convective-heat-transfer coefficient. The thermal resistances, R_1 and R_2 , both have units of ($^\circ\text{C W}^{-1}$) or (K W^{-1}). R_1 and R_2 from Eqs. (1) and (2) indicate that they are determined by material properties and are independent of the amount of the supplied power (q). However, in reality, R_1 and R_2 may vary depending on q because ΔT and q are nonlinear due to a three dimensional nature of the heating wire over a flat plane. This nonlinearity between ΔT and q causes a shift in thermal resistance as $R \sim \Delta T/q$. By equating Eqs. (1) and (2), the following expression is obtained:

$$q = \frac{T_1 - T_\infty}{\sum R_i} = \frac{T_1 - T_\infty}{R_1 + R_2}. \quad (3)$$

Equations (1) and (2) can be rearranged as shown below,

$$R_1 = (T_1 - T_2) \cdot q^{-1}, \quad (4)$$

$$R_2 = (T_2 - T_\infty) \cdot q^{-1}. \quad (5)$$

Equations (4) and (5) are used to estimate R_1 and R_2 using the measured T_1 , T_2 , and q values. It should be noted that q is a relative value from the power reading, as $q = I \cdot V$, wherein the electrical current (I) and applied voltage (V) are measured. The actual heat flux (q_{actual}) that the heating wire releases may be considerably smaller, considering the power loss through the heating system. The method of estimating q_{actual} is discussed hereinafter. At present, the value of q from the power reading is used for relative comparison.

The quasi-1D analysis based on Fourier's law and Newton's cooling law indicated that heat from the linear wire source spread not only in the "normal" (axial) direction, but also in the "in-plane" (radial) and azimuthal directions, presenting a three-dimensional phenomenon. However, to simplify the model, heat transfer in the normal direction was assumed to be dominant. In addition, the substrate bottom was well-insulated, and, therefore, it was assumed that heat flowed only in the normal direction. The heat loss through radiation was assumed to be negligible because the temperature of the film surface remained below 120°C .

Figure 6(b) presents a comparison of the thermal resistances, R_1 , for the films of various thicknesses: $N = 0, 5, 10$, and 20 . The thermal resistances from all values of q (9, 12, 15, and 18) were averaged to represent R_1 in Fig. 6(b). When $N = 0$, corresponding to the bare alumina substrate without any CNTs, R_1 was relatively high. With thicker CNT layers ($N = 5$ and 10), R_1 declined, confirming that adding the CNTs increases the ability of the coated layer to increase the overall thermal conductivity. When $N = 20$, R_1 again increased substantially because the excessively thick coating layer behaved more like a thermal insulator. Figure 6(c) presents a comparison of the R_2 values for all cases of N . R_2 represents the effectiveness of the thermal resistance from the upper surface of the film to the open air and R_2 is related to the effectiveness of convection. Convection cooling became more effective with increasing N because of the enhanced texturing effect. The resistance in the convection, R_2 , decreased from $N = 0$ to $N = 5$ owing to the surface texturing. Greater texturing by depositing more CNTs (moving from

$N = 5$ to $N = 10$) induced a greater reduction in R_2 . However, at $N = 20$, the thermal-insulation effect became dominant, thereby increasing both T_1 and T_2 , which, in turn, increased R_1 and R_2 ; see Eqs. (4) and (5). Overall, adding the CNTs increased both the thermal conductivity and the effective convection cooling, up to a reasonable thickness; herein $N = 10$ was found to be the optimal thickness, as shown in Fig. 6(d). When the coating layer was excessively thick, the thermal resistance again increased, leading to an adverse effect.

Figure 7(a) presents a comparison of the thermal resistances (R_1 and R_2) of the bare substrate ($N = 0$), CNTs ($N = 10$), and CNT/AgNW ($N = 10$) films. Addition of the CNTs certainly enhanced the thermal conductivity and thus reduced R_1 , as opposed to the case for the bare substrate. Further addition of the AgNWs to the CNTs yielded no significant improvement in R_1 , suggesting that the overall thermal conductivity did not change with addition of the AgNWs. However, adding the AgNWs visibly improved R_2 , as shown in Fig. 7(a). Because R_2 is a measure of convection, a lower R_2 value indicates that convection cooling became more effective with the enhanced texturing. The length scale of the AgNWs is comparable to that of the CNTs at approximately 10 nm , where the thickness of the resulting hybrid films was in the range of $5\text{--}15\ \mu\text{m}$. The nano-scale texturing derived from the introduction of the AgNWs indeed

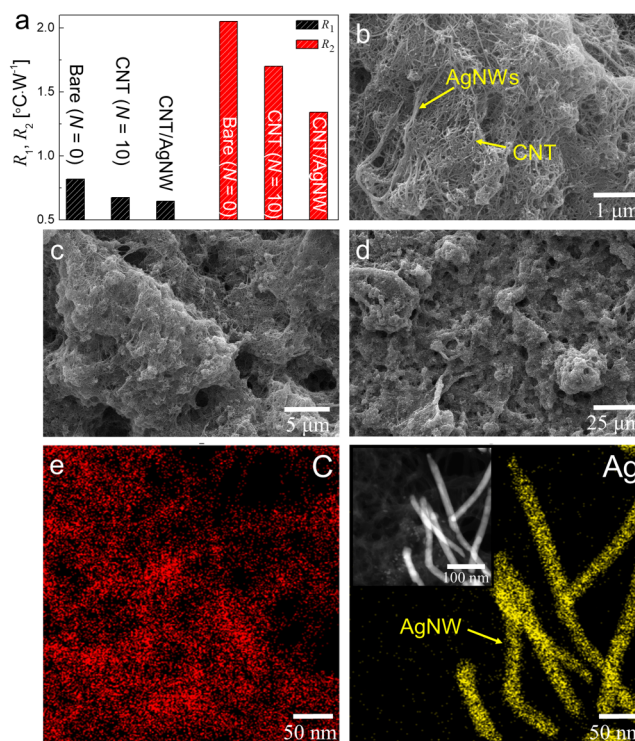


FIG. 7. (a) Thermal resistance (R_1 and R_2) of the hybrid film consisting of CNTs and AgNWs ($N = 10$) shown in the multi-scaled SEM images in (b)–(d), and (e) elemental mapping images of C (left; red) and Ag (right; yellow), and low-magnification TEM image (inset).

TABLE I. Comparison of effective heat-transfer-coefficients (h_{eff}) of CNT and CNT/AgNW films when $q = I \cdot V = 18 \text{ W}$. The actual power (q_{actual}) was estimated to be 0.87 W .

Material	h_{eff} ($\text{W m}^{-2} \text{K}^{-1}$)	h_{eff}^{-1} or $R_2 \cdot A_p$ ($\text{m}^2 \text{K W}^{-1}$)	R_2 (K W^{-1})
CNT ($N = 0$)	1.83	0.55	55
CNT ($N = 5$)	1.89	0.53	53
CNT ($N = 10$)	2.18	0.46	46
CNT ($N = 20$)	2.02	0.50	50
CNT/AgNW ($N = 10$)	2.45	0.41	41

reduced R_2 . The morphological distinction between the CNTs and AgNWs is difficult to observe because both species are cylindrical and have a similar length scale [Fig. 7(b)]. The morphology of the CNT/AgNW mixture in multi-scales is shown in Figs. 7(c) and 7(d). The structure and morphology of the CNT/AgNW film were also investigated by TEM. The EDS elemental mapping data for carbon and silver in the fabricated film are shown in Fig. 7(e). These images confirm that both C and Ag were uniformly distributed over the film surface and were readily discernable. The inset image in Fig. 7(e) shows the low-magnification TEM image of the AgNWs, demonstrating the inclusion of AgNW in the hybrid film.

Table I presents a comparison of the effective heat-transfer-coefficients (h_{eff}) in units of ($\text{W m}^{-2} \text{K}^{-1}$), and the reciprocal, $1/h_{\text{eff}}$, in units of ($\text{m}^2 \text{K W}^{-1}$), which is also known as the specific thermal resistance, ($R_2 \cdot A_p$). The convective thermal resistance, R_2 , values listed in Table I should not be compared with the values reported in Fig. 6(c) because herein, the actual heat, q_{actual} (0.87 W) was used instead of the electrical power reading of $q = I \cdot V = 18 \text{ W}$. To estimate h_{eff} , the actual heat released by the heating power must be used,

$$h_{\text{eff}} = \frac{q_{\text{actual}}}{A_p(T_2 - T_{\infty})}, \quad (6)$$

where q_{actual} , the actual heat released by the Ni-Cr wire, can be estimated using the equation below,

$$q_{\text{actual}} = h_b A_w (T_1 - T_{\infty}). \quad (7)$$

Here, the surface area of the cylindrical wire, A_w , can be calculated as $A_w = \pi dL$, where d and L are the diameter ($d = 1 \text{ mm}$) and length of the wire ($L = 0.12 \text{ m}$), respectively, and h_b is the heat-transfer coefficient of the bare alumina substrate at $T_1 = 92.2 \text{ }^\circ\text{C}$ and $T_{\infty} = 28 \text{ }^\circ\text{C}$. Moreover, h_b was obtained using the Nusselt number, Nu , as follows: $h_b = Nu k / d$, where k is the thermal conductivity of air. Furthermore, k was determined to be $k = 0.02881 \text{ W m}^{-1} \text{K}^{-1}$ using

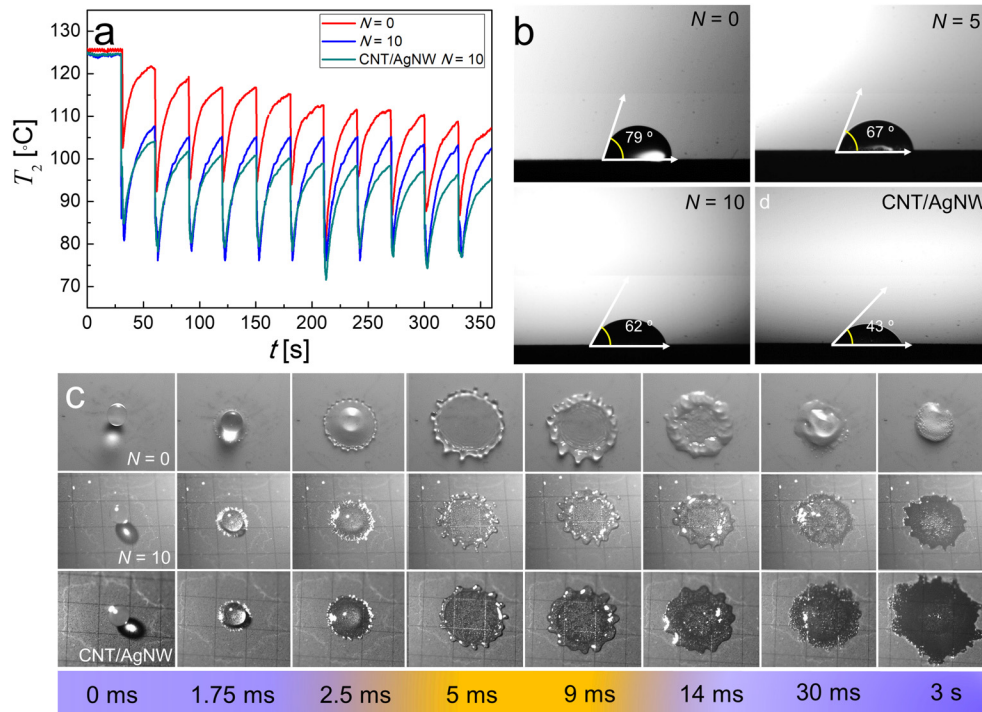


FIG. 8. (a) Changes in surface temperature (T_2) during spray-cooling for various films; initially, the heater temperature was $T_h = 130 \text{ }^\circ\text{C}$. Water contact angles for (b) $N = 0$ (bare), $N = 10$ (CNT only), and $N = 10$ (CNT/AgNW) films at $T_2 = T_{\infty} = 28 \text{ }^\circ\text{C}$. (c) Drop impact on $N = 0$ (bare), $N = 10$ (CNT only), and $N = 10$ (CNT/AgNW) films (in order from top to bottom) at $T_h = 130 \text{ }^\circ\text{C}$.

the film temperature, T_f , where $T_f = (T_1 + T_\infty)/2 = 60.1^\circ\text{C} = 333.1\text{K}$. For the natural convection of air from a horizontal cylinder (heating wire), Nu can be calculated using the Grashof (Gr) and Prandtl (Pr) numbers, as follows:

$$\text{Gr Pr} = g\beta(T_s - T_\infty)d^3 \text{Pr}/\nu^2 \quad (8)$$

and

$$\text{Nu} = 1.02(\text{Gr} \cdot \text{Pr})^{0.148}, \quad (9)$$

where g is the gravitational acceleration ($g = 9.81\text{ m s}^{-2}$); β is the thermal-expansion coefficient of air, which is defined as $\beta = T_f^{-1} = 0.003\text{ K}^{-1}$; and ν is the kinematic viscosity of air at T_f . Here, $\text{Pr} = 0.7202$ and $\nu = 0.0001896\text{ m}^2\text{ s}^{-1}$ at $T_f = 60.1^\circ\text{C}$. When h_b , A_w , and $(T_1 - T_\infty)$ are known, q_{actual} can be calculated using Eq. (7), and in the present case, $q_{\text{actual}} = 0.87\text{ W}$. The actual values of h_{eff} , which were subsequently calculated using Eq. (6), are listed in Table I.

The data in Table I indicate that the CNT/AgNW film produced an approximately 34% improvement in h_{eff} , compared with that of the bare substrate ($N = 0$). Compared with the bare substrate, h_{eff} was 19% higher for the pure CNTs ($N = 10$ without AgNWs). This improvement allowed us to reduce the wire temperature (T_1) by 7–15°C, which provided significant flexibility in addressing the thermal stress induced by hotspots. Table II compares the thermal conductivity of hybrid heat spreaders comprising materials similar to the CNT-AgNW synthesized in the present study. The film thermal resistance in the in-plane direction is in

the order of $\sim 10^{-6}\text{ m}^2 \times \text{K} \times \text{W}^{-1}$ while that in the normal direction is in the order of $\sim 10^{-3}\text{ m}^2 \times \text{K} \times \text{W}^{-1}$. Among them, our CNT-AgNW composite has the lowest normal thermal resistance, which demonstrates its superior heat spreading capability.

Figure 8(a) illustrates the spray-cooling phenomenon for the fabricated $N = 0$ (bare), $N = 10$ (CNT only), and $N = 10$ (CNT/AgNW) films. These three films were simultaneously sprayed with liquid droplets. The surface temperature (T_2) of the films declined sharply as the liquid droplets evaporated, during which latent heat was extracted from the heated surface. T_2 again increased as soon as all of the liquid droplets evaporated with the continuous supply of heat to the surface. This spray-cooling cycle was performed 11 times over a duration of 360 s, during which T_2 gradually declined. Among the tested cases, the CNT/AgNW hybrid film exhibited the best cooling performance because of its superior wettability. Figure 8(b) shows the static wettability of the various films, wherein the CNT/AgNW composite was confirmed to be the most hydrophilic. In this case, the sprayed liquid droplets adhered strongly to the surface, which promoted strong contact between the droplets and the surface, resulting in efficient heat transfer. Figure 8(c) shows the time-series snapshots illustrating the dynamic wettability of an impacted droplet having a diameter of $D_0 = 3\text{ mm}$ and a released height of $H = 18\text{ cm}$. These time-series snapshots also suggest that the CNT/AgNW film exhibited the highest wettability during the dynamic impact test. Figure 8(c) shows the occurrence of droplet spreading and recoiling. In general, a droplet spreads upon impact and reaches the maximum diameter and then recoils owing to surface tension. The snapshots for the $N = 0$ (bare) film in Fig. 8(c) demonstrate the typical

TABLE II. Comparison of the thermal conductivity (k) of hybrid heat spreaders comprising materials similar to the CNT-AgNW synthesized in the present study.

Materials	k ($\text{W m}^{-1}\text{ K}^{-1}$)	Δx (m)	Film thermal resistance ($\text{m}^2\text{ K W}^{-1}$)	Testing method	Reference
CNT-AgNW	0.11	1.0×10^{-4}	0.9×10^{-3}	ASTM E1461	Present study (normal)
GnP	0.23	1.0×10^{-3}	4.35×10^{-3}	Hot-wire	47 (normal)
Carbon nanofiber	1.85	1.0×10^{-2}	5.4×10^{-3}	Hot Disk AB	48 (normal)
rGO-AgNW	0.08	1.0×10^{-4}	1.25×10^{-3}	ASTM E1461	49 (normal)
2.4 vol. % GNP	0.476	...	62×10^{-6}		50 (in-plane)
GnP	1.4	...	$\sim 1.0 \times 10^{-6}$	ASTM C177	51 (in-plane)
Penetrated flexible graphite	3.8	...	1.3×10^{-6}	ASTM D5470	52 (in-plane)
Graphene-MLG	14	...	71×10^{-6}	Laser flash (NETZSCH)	26 (in-plane)
Graphene-fabric	3.73	1.2×10^{-4}	32×10^{-6}	Laser flash (NETZSCH)	53 (in-plane)
Graphene oxide	0.92	2.0×10^{-5}	21×10^{-6}	ASTM D-5470	54 (in-plane)

droplet-impact scenario, comprising spreading, fingering, and recoiling. However, for the $N=10$ (CNT) film, the textured surface promoted strong adherence of the liquid droplet to the surface through the formation of the Wenzel state, in which the liquid is pinned at roughened surfaces. The liquid is imbibed into the roughened surface and anchored to the surface, which prevents recoiling of the liquid film.⁴⁶ The CNT/AgNW film surface was more hydrophilic than the surface of the $N=10$ (CNT) film, and the recoiling motion was completely suppressed, which produced the largest spreading diameter and hence, the thinnest liquid film. In such a scenario, evaporation is expedited because of the larger coverage area of the liquid film at the same constant heat flux. As a result, the liquid is subjected to more heat, and thus evaporates faster (Table II).

IV. CONCLUSION

Hybrid films comprising CNTs and AgNWs were used as cooling films for applications in high-power-density electronics. Inclusion of the CNT/AgNW enhanced the thermal conductivity of the film, which, in turn, lowered the overall thermal resistance of the film. The supersonically sprayed CNTs produced a highly textured surface, thereby increasing the convective-heat-transfer cooling by increasing the surface area. Addition of the AgNWs further increased the convective heat transfer coefficient by increasing the surface area via texturing. The CNT/AgNW hybrid film also exhibited increased wettability owing to the formation of the Wenzel state, which ensured strong adhesion, imbibition, and larger spreading of the impacting liquid droplets. Consequently, evaporative cooling was augmented owing to the enhanced heat transfer between the liquid droplets and the heated surface.

AUTHORS' CONTRIBUTIONS

T.-G.K. and C.-W.P. have contributed equally to this work.

ACKNOWLEDGMENTS

This research was supported by the Technology Development Program to Solve Climate Changes of the National Research Foundation (NRF) funded by the Ministry of Science, ICT and Future Planning (No. NRF-2016M1A2A2936760) and by the Advanced Research Center Program (No. NRF-2013R1A5A1073861). This research was funded by the Deanship of Scientific Research at the King Saud University (Research Group No. RG-1438-038).

REFERENCES

- ¹H. Zhang, S. Shao, H. Xu, H. Zou, and C. Tian, *Renew. Sustain. Energy Rev.* **35**, 171 (2014).
- ²S. T. Kadam and R. Kumar, *Int. J. Therm. Sci.* **85**, 73 (2014).
- ³A. C. Kheirabadi and D. Groulx, *Appl. Therm. Eng.* **105**, 622 (2016).
- ⁴E. Sevinchan, I. Dincer, and H. Lang, *Appl. Therm. Eng.* **140**, 799 (2018).
- ⁵M. Iyengar and R. Schmidt, in *Analytical Modeling for Prediction of Hot Spot Chip Junction Temperature for Electronics Cooling Applications* (IEEE, 2006), p. 87.
- ⁶P. Wang and A. Bar-Cohen, *J. Appl. Phys.* **102**, 034503 (2007).
- ⁷A. L. Moore and L. Shi, *Mater. Today* **17**, 163 (2014).
- ⁸A. Majumdar, *Nat. Nanotechnol.* **4**, 214 (2009).
- ⁹B. Yang, P. Wang, and A. Bar-Cohen, *IEEE Trans. Compon. Packag. Technol.* **30**, 432 (2007).

- ¹⁰T. Cader and D. Tilton, in *Implementing Spray Cooling Thermal Management in High Heat Flux Applications* (IEEE, 2004), p. 699.
- ¹¹T. Harman, P. Taylor, M. Walsh, and B. LaForge, *Science* **297**, 2229 (2002).
- ¹²R. Venkatasubramanian, E. Siivola, T. Colpitts, and B. O'quinn, *Nature* **413**, 597 (2001).
- ¹³X. Fan, G. Zeng, C. LaBounty, J. E. Bowers, E. Croke, C. C. Ahn, S. Huxtable, A. Majumdar, and A. Shakouri, *Appl. Phys. Lett.* **78**, 1580 (2001).
- ¹⁴R. S. Prasher, J.-Y. Chang, I. Sauciu, S. Narasimhan, D. Chau, G. Chrysler, A. Myers, S. Prstic, and C. Hu, *Intel Technol. J.* **9**, 285–296 (2005).
- ¹⁵A. Bar-Cohen and P. Wang, *Microgravity Sci. Technol.* **21**, 351 (2009).
- ¹⁶I. Chowdhury, R. Prasher, K. Lofgreen, G. Chrysler, S. Narasimhan, R. Mahajan, D. Koester, R. Alley, and R. Venkatasubramanian, *Nat. Nanotechnol.* **4**, 235 (2009).
- ¹⁷Z. J. Zuo, M. T. North, and K. L. Wert, *IEEE Trans. Compon. Packag. Technol.* **24**, 220 (2001).
- ¹⁸Z. Rao, S. Wang, M. Wu, Z. Lin, and F. Li, *Energy Convers. Manage.* **65**, 92 (2013).
- ¹⁹A. Greco, D. Cao, X. Jiang, and H. Yang, *J. Power Sources* **257**, 344 (2014).
- ²⁰S. An, H. S. Jo, S. S. Al-Deyab, A. L. Yarin, and S. S. Yoon, *J. Appl. Phys.* **119**, 065306 (2016).
- ²¹S. Gelin, H. Tanaka, and A. Lemaître, *Nat. Mater.* **15**, 1177 (2016).
- ²²T. Zhu, K. Swaminathan-Gopalan, K. J. Cruse, K. Stephani, and E. Ertekin, *Adv. Funct. Mater.* **28**, 1706268 (2018).
- ²³T. Zhu and E. Ertekin, *Nano Lett.* **16**, 4763 (2016).
- ²⁴G.-C. He, H. Lu, X.-Z. Dong, Y.-L. Zhang, J. Liu, C.-Q. Xie, and Z.-S. Zhao, *RSC Adv.* **8**, 24893 (2018).
- ²⁵S. Ghosh, I. Calizo, D. Teweldebrhan, E. P. Pokatilov, D. L. Nika, A. A. Balandin, W. Bao, F. Miao, and C. N. Lau, *Appl. Phys. Lett.* **92**, 151911 (2008).
- ²⁶K. M. Shahil and A. A. Balandin, *Solid State Commun.* **152**, 1331 (2012).
- ²⁷K. M. Shahil and A. A. Balandin, *Nano Lett.* **12**, 861 (2012).
- ²⁸Q. Q. Kong, Z. Liu, J. G. Gao, C. M. Chen, Q. Zhang, G. Zhou, Z. C. Tao, X. H. Zhang, M. Z. Wang, and F. Li, *Adv. Funct. Mater.* **24**, 4222 (2014).
- ²⁹N.-J. Song, C.-M. Chen, C. Lu, Z. Liu, Q.-Q. Kong, and R. Cai, *J. Mater. Chem. A* **2**, 16563 (2014).
- ³⁰M. Shtein, R. Nadviv, M. Buzaglo, and O. Regev, *ACS Appl. Mater. Interfaces* **7**, 23725 (2015).
- ³¹Y. Zhang, H. Han, N. Wang, P. Zhang, Y. Fu, M. Murugesan, M. Edwards, K. Jeppson, S. Volz, and J. Liu, *Adv. Funct. Mater.* **25**, 4430 (2015).
- ³²J. Xu, A. Munari, E. Dalton, A. Mathewson, and K. M. Razeeb, *J. Appl. Phys.* **106**, 124310 (2009).
- ³³H. Yu, L. Li, T. Kido, G. Xi, G. Xu, and F. Guo, *J. Appl. Polym. Sci.* **124**, 669 (2012).
- ³⁴K. Sanada, Y. Tada, and Y. Shindo, *Compos. Part A* **40**, 724 (2009).
- ³⁵T. Zhang, B. G. Sammakia, Z. Yang, and H. Wang, *J. Electron. Packag.* **140**, 031006 (2018).
- ³⁶A. Yu, P. Ramesh, M. E. Itkis, E. Bekyarova, and R. C. Haddon, *J. Phys. Chem. C* **111**, 7565 (2007).
- ³⁷M. A. Peacock, C. K. Roy, M. C. Hamilton, R. W. Johnson, R. W. Knight, and D. K. Harris, *Int. J. Heat Mass Transf.* **97**, 94 (2016).
- ³⁸J.-G. Lee, S. An, T.-G. Kim, M.-W. Kim, H.-S. Jo, M. T. Swihart, A. L. Yarin, and S. S. Yoon, *ACS Appl. Mater. Interfaces* **9**, 35325 (2017).
- ³⁹J.-G. Lee, J.-H. Lee, S. An, D.-Y. Kim, T.-G. Kim, S. S. Al-Deyab, A. L. Yarin, and S. S. Yoon, *J. Mater. Chem. A* **5**, 6677 (2017).
- ⁴⁰T.-G. Kim, E. Samuel, B. Joshi, C.-W. Park, M.-W. Kim, M. T. Swihart, W. Y. Yoon, and S. S. Yoon, *J. Alloys Compd.* **766**, 331 (2018).
- ⁴¹S. An, B. Joshi, A. L. Yarin, M. T. Swihart, and S. S. Yoon, *Adv. Mater.* **32**, e1905028 (2019).
- ⁴²D. Y. Kim, S. Sinha-Ray, J. J. Park, J. G. Lee, Y. H. Cha, S. H. Bae, J. H. Ahn, Y. C. Jung, S. M. Kim, and A. L. Yarin, *Adv. Funct. Mater.* **24**, 4986 (2014).
- ⁴³J. G. Lee, D.-Y. Kim, J.-H. Lee, M.-W. Kim, S. An, H. S. Jo, C. Nervi, S. S. Al-Deyab, M. T. Swihart, and S. S. Yoon, *ACS Appl. Mater. Interfaces* **8**, 15406 (2016).

- ⁴⁴J. G. Lee, D. Y. Kim, J. H. Lee, S. Sinha-Ray, A. L. Yarin, M. T. Swihart, D. Kim, and S. S. Yoon, *Adv. Funct. Mater.* **27**, 1602548 (2017).
- ⁴⁵S. J. Kline, *Mech. Eng.* **75**, 3 (1953).
- ⁴⁶K. Kubiak, M. Wilson, T. Mathia, and P. Carval, *Wear* **271**, 523 (2011).
- ⁴⁷M.-T. Hung, O. Choi, Y. S. Ju, and H. Hahn, *Appl. Phys. Lett.* **89**, 023117 (2006).
- ⁴⁸M. A. Raza, A. Westwood, and C. Stirling, *Carbon* **50**, 84 (2012).
- ⁴⁹T.-G. Kim, C.-W. Park, D.-Y. Woo, J. Choi, and S. S. Yoon, *Appl. Therm. Eng.* **165**, 114572 (2020).
- ⁵⁰C. Lin and D. Chung, *Carbon* **47**, 295 (2009).
- ⁵¹M. Raza, A. Westwood, and C. Stirling, in *Graphite Nanoplatelet/Silicone Composites for Thermal Interface Applications* (IEEE, 2010), p. 34.
- ⁵²K. Hu and D. Chung, *Carbon* **49**, 1075 (2011).
- ⁵³J. Gong, Z. Liu, J. Yu, D. Dai, W. Dai, S. Du, C. Li, N. Jiang, Z. Zhan, and C.-T. Lin, *Compos. Part A* **87**, 290 (2016).
- ⁵⁴I. H. Tseng, J. C. Chang, S. L. Huang, and M. H. Tsai, *Polym. Int.* **62**, 827 (2013).